MNRAS 000, 1–?? (2018) Preprint 1 February 2022 Compiled using MNRAS LATEX style file v3.0

Rings and arcs around evolved stars. II. The Carbon Star AFGL 3068 and the Planetary Nebulae NGC 6543, NGC 7009 and NGC 7027

M.A. Guerrero[1]⋆, G. Ramos-Larios[2], J.A. Toalá[3], B. Balick[4], and L. Sabin[5]
[1]*Instituto de Astrofísica de Andalucía (IAA-CSIC), Glorieta de la Astronomía S/N, 18008 Granada, Spain*
[2]*Instituto de Astronomía y Meteorología, Universidad de Guadalajara, Av. Vallarta 2602, Arcos Vallarta, 44130 Guadalajara, Mexico*
[3]*Instituto de Radioastronomía y Astrofísica (IRyA), UNAM Campus Morelia, Apartado postal 3-72, 58090 Morelia, Michoacan, Mexico*
[4]*Department of Astronomy, University of Washington, Seattle, WA 98195-1580, USA*
[5]*Instituto de Astronomía, Universidad Nacional Autónoma de México, Apdo. Postal 877, 22860 Ensenada, B. C., Mexico*

1 February 2022

ABSTRACT

We present a detailed comparative study of the arcs and fragmented ring-like features in the haloes of the planetary nebulae (PNe) NGC 6543, NGC 7009, and NGC 7027 and the spiral pattern around the carbon star AFGL 3068 using high-quality multi-epoch *HST* images. This comparison allows us to investigate the connection and possible evolution between the regular patterns surrounding AGB stars and the irregular concentric patterns around PNe. The radial proper motion of these features, $\simeq$15 km s^{-1}, are found to be consistent with the AGB wind and their linear sizes and inter-lapse times (500 – 1900 yr) also agree with those found around AGB stars, suggesting a common origin. We find evidence using radiative-hydrodynamic simulations that regular patterns produced at the end of the AGB phase become highly distorted by their interactions with the expanding PN and the anisotropic illumination and ionization patterns caused by shadow instabilities. These processes will disrupt the regular (mostly spiral) patterns around AGB stars, plausibly becoming the arcs and fragmented rings observed in the haloes of PNe.

Key words: stars: evolution — stars: winds, outflows — stars: carbon — planetary nebulae: individual: AFGL 3068, NGC 6543, NGC7009, and NGC 7027

1 INTRODUCTION

Back in the mid 80s, planetary nebulae (PNe) were still considered to be single shells of ionized material resulting from a massive episode of mass-loss marking the end of the asymptotic giant branch (AGB) phase (the so-called superwind) during the late evolution of low- and intermediate-mass (1 M$_\odot$ $\lesssim$ M$_{\rm i}$ $\lesssim$8 M$_\odot$) stars. The discovery of extended haloes, low surface-brightness detached shells, and the identification of attached shells surrounding the bright main nebulae (Chu et al. 1987; Frank et al. 1990; Balick et al. 1992) revealed them as multi-layered shells of gas, each shell providing us with information on different episodes of mass-loss in the late evolution of AGB stars (Stanghellini & Pasquali 1995).

Accordingly, a PN can consist of different shells, including from inside out a hot bubble and bright nebular rim, a nebular envelope and a halo. The nebular envelope is attributed to the superwind, a dense, slow, and most-likely neutral wind, which produces dusty shells that enshroud the central star (e.g., Cox et al. 2012; Mauron et al. 2013, and references therein). As the post-AGB star increases its temperature and subsequently its ionizing flux, the nebular shell is rapidly (or nearly instantly) photo-ionized, producing a sharp increase of the thermal pressure inside. At the same time, the post-AGB star develops a fast stellar wind that pushes outwards on the nebular envelope, producing a sharp rim of swept-up material, whereas the fast stellar wind is shock-heated and reaches X-ray-emitting temperatures, producing a hot bubble that can be detected through its diffuse X-ray emission (e.g., Chu et al. 2001; Guerrero et al. 2002; Kastner et al. 2001). Because of the dynamical effects of these processes, the signatures from the previous mass loss history are mostly erased. Finally, the haloes are attributed to the last thermal pulse experienced by the AGB star before leaving this phase (Stanghellini & Pasquali 1995; Guerrero & Manchado 1999).

In the late 90s, a new PN structural component was added to this list: concentric, ring-like features or arcs detected immediately outside their bright inner nebular shells. Actually, these ring-like structures were first reported in dust-scattered *Hubble Space Telescope (HST)* images of the proto-PNe (extended sources just evolving into the PN stage) CRL 2688, IRAS 17150−3224, and IRAS 17441−2411 (Kwok et al. 1998; Sahai et al. 1998; Su et al. 1998), and immediately after in the PNe Hubble 5, NGC 7027,

⋆ E-mail: mar@iaa.es

Table 1. General information of the sources in our sample

Source	RA (J2000)	DEC (J2000)	Distance (kpc)	T_{eff} (K)	Spectral Type
AFGL 3068	23 19 12.6	+17 11 33.1	1.0	2200	Carbon Star
NGC 6543	17 58 33.4	+66 37 58.7	1.63±0.19	63000	Of-WR(H)
NGC 7009	21 04 10.8	−11 21 48.5	1.15±0.15	82000	O(H)
NGC 7027	21 07 01.8	+42 14 10.0	1.0	215000	...

and the very remarkable case of NGC 6543 (Terzian & Hajian 2000; Balick et al. 2001). Later *HST* and ground-based optical and space mid-infrared *Spitzer* images of emission lines from ionized gas or continuum emission scattered by dust have found an increasing number of them (e.g. Corradi et al. 2004; Ramos-Larios et al. 2011; Gómez-Muñoz et al. 2015, and references therein). In Ramos-Larios et al. (2016, hereafter Paper I), ring-like features were searched systematically in a sample of ~650 PNe and proto-PNe with suitable *HST* and *Spitzer* archival images. These features were found to be ubiquitous to all types of nebular morphologies, but present only in a reduced ≃8% fraction of sources. For consistency with Paper I, we will generically refer to these arcs and fragmented rings as *rings*, even though their shapes can only approximately and locally be fitted by concentric circles.

The large angular size and low-surface brightness of these ring-like features have hampered their characterisation. Balick et al. (2001) presented a detailed analysis of the rings in NGC 6543, a.k.a. the Cat's Eye Nebula, using *HST* images, concluding that they have a thickness of ~1000 AU and an ejection time-lapse of 1500 yr. The optical and mid-infrared study of IC 418 presented by Ramos-Larios et al. (2012) confirmed ejection time lapses of the same order ~630 yr for the three concentric rings surrounding the bright main nebula. The clear ring-like structures around CRL 618 and CRL 2688 offer a unique opportunity to investigate this phenomenon among proto-PNe. A comprehensive investigation of the formation of the proto-PN CRL 2688 using multi-epoch *HST* observations (Balick et al. 2012) implied proper motions of 0.″011 yr^{-1} for the rings, from which ejection time-lapses of 100 yr during the last 4000 yr with an almost constant ejection velocity of 18 km s^{-1} are derived. A similar investigation, however, yielded inconclusive results for the rings around the proto-PN CRL 618 (Balick el al. 2013).

The origin of ring-like structures in PNe and proto-PNe is the result of sustained, thousand-year quasi-periodic instabilities in the poorly understood AGB wind ejection process. Different scenarios have been proposed to address their formation, including i) viscous momentum (de)coupling between outflowing gas and dust (e.g. Simis et al. 2001), ii) solar-like magnetic inversions (e.g. García-Segura et al. 2001), iii) periastron passage of a stellar companion (e.g. Harpaz et al. 1997), and iv) variability in the wind of the AGB progenitor (e.g. Zijlstra et al. 2002), to mention a few. Still, our current knowledge of the formation and evolution of these features among PNe and proto-PNe is not complete, but the answers should be looked for in the previous stage of the stellar evolution, during the late AGB phase.

Detailed mapping of the AGB circumstellar dust distribution in scattered light at optical wavelengths has produced conspicuous results, including the detection of the first detached shell and spiral structure around the carbon-rich AGB stars TT Cyg (Olofsson et al. 1998) and AFGL 3068 (Mauron & Huggins 2006), respectively. Subsequent sub-millimeter observations have detected many other cases of regular patterns around AGB stars (e.g., Olofsson et al. 1996; Mayer, et al. 2013; Dinh-V.-Trung & Lim 2009) and even peered into the velocity field of amazing 3D spiral patterns (e.g., Maercker et al. 2012; Cernicharo et al. 2015; Kim et al. 2017). Currently, the most accepted scenario for the formation of spirals around AGB stars is that of binary interactions, where a binary companion in a highly eccentric orbit influences the spherical AGB wind to imprint a spiral structure (Mastrodemos & Morris 1999). More recent detailed hydrodynamic simulations support those early results (Kim, Liu & Taam 2019, and references therein).

It is intriguing that the regular spiral patterns observed occasionally among AGB stars are not detected around evolved sources such as proto-PNe and PNe (paper I). This indicates that the ring-like features detected in PNe and proto-PNe are either not related to the regular mass-loss patterns of AGB stars, or that the regular AGB patterns are altered or even destroyed at some point of the subsequent PN formation and evolution. To investigate these possibilities, this paper presents a comparative study of the geometry, surface brightness variations and angular expansion of the ring-like structures of three bright, relatively nearby and mature PNe with high-quality multi-epoch *HST* observations, namely NGC 6543, NGC 7009, and NGC 7027, with those of the spiral structure around the AGB star AFGL 3068. This study is complemented by radiative-hydrodynamic simulations to assess the effects of the evolving stellar wind and ionizing flux during the post-AGB phase on regular patterns produced just at the end of the AGB phase. The present paper is organised as follows. Section 2 describes the four objects and the *HST* observations used here, Section 3 investigates the geometry of the ring-like features of these PNe and compares them to the spiral structure of AFGL 3068, and Section 4 uses multi-epoch *HST* observations to investigate the evolution in time of the surface brightness of these features and their expansion velocity. Finally, a discussion on the evolution during the post-AGB phase of regular patterns resulting from the last gasps of the AGB wind is presented in Section 5 and some general concluding remarks are laid down in Section 6.

2 ARCHIVAL DATA AND SAMPLE DESCRIPTION

Our previous investigations of ring-like features in proto-PNe and PNe (paper I) has allowed us to select three PNe, namely NGC 6543, NGC 7009, and NGC 7027, with multi-epoch *HST* images of sufficient quality to detect and trace faint ring-like features around their main nebular shells and with a time-span adequate to determine their expansion. The properties of these three PNe, and these of the carbon star AFGL 3068, are presented in Table 1. *HST* images of these sources were downloaded from the Hubble Legacy Archive

Table 2. Description of the *HST* datasets used for analysis

Source	Detector	Aperture	Filter	Date	Exposure time (s)	Program	Purpose
AFGL 3068	ACS/WFC	WFC1	F606W	2004-09-18	1388	10185	EXP
AFGL 3068	ACS/WFC	WFC1	F606W	2010-10-20	9804	11676	IMG,SB,EXP
NGC 6543	WFPC2	PC1	F502N	1994-09-18	1600	5403	EXP
NGC 6543	WFPC2	PC1	F502N	2000-09-15	1200	8390	EXP
NGC 6543	ACS/WFC	WFC	F502N	2002-05-04	700	9026	IMG,SB
NGC 7009	WFPC2	WF3	F502N	2000-04-07	320	8114	IMG
NGC 7027	WFPC2	PC1	F555W	1995-08-21	300	6119	IMG
NGC 7027	WFPC2	PC1	F555W	2008-08-13	260	11122	IMG,EXP

at the Mikulski Archive for Space Telescopes (MAST)[1] to obtain a description of their morphological features and to investigate their angular expansion. Details of the observations used in this paper are listed in Table 2. According to the keywords listed in the "Purpose" column of this table, the observations were used to prepare the images presented in this paper (IMG), to build surface brightness profiles (SB), or to investigate the angular expansion (EXP). To avoid any instrumental effects, the investigation of the angular expansion has been carried out using only observations obtained with the same *HST* camera and filter.

Figure 1 shows high-quality colour-composite images of these four objects. Layers, masks and unsharp masking techniques were applied to the images presented in this figure to enhance the weak ring-like structures, but we note that these images are not used to extract any quantitative information besides the spatial distribution of the ring-like features. In particular, the image presented here for NGC 7009 is a composition of a *HST* WFPC2 picture for the inner shell and a Very Large Telescope (VLT) MUSE picture for the envelope and the ring-like external features. The most obvious structural component in AFGL 3068 is a spiral pattern, with up to seven turns. The spatial distribution of this dust-scattered emission follows an Archimedean spiral (Mauron & Huggins 2006), which extends even closer to the central source in sub-mm CO observations (Kim et al. 2017). Lacking a fast stellar wind, there is no bright inner shell in AFGL 3068, contrary to NGC 6543, NGC 7009 and NGC 7027, whose central stars current fast stellar winds have carved inner cavities into their nebular envelopes.

3 GEOMETRY OF THE RINGS

The comparison between the shape of the ring-like features around proto-PNe and PNe and the regular patterns around AGB stars can help us elucidate whether there is an evolutionary link between these morphological structures. The pattern around AFGL 3068 (top-left panel of Fig. 1) certainly portrays a spiral, whereas the ring-like features around the three PNe in the remaining panels in Figure 1 cannot be described neither as circular nor as spiral, in agreement with the conclusions presented in Paper I.

These statements are substantiated in Figure 2, which shows the *HST* images of these sources in polar (r, θ) coordinates. The polar image of AFGL 3068 (Fig. 2-top) clearly shows the signature of an Archimedean spiral pattern, for which the radius of each emission features increases almost linearly with the angular coordinate θ (the dotted yellow line in Fig. 2). This spiral pattern extends from $3\farcs4$ up to $17\farcs4$ from the position of AFGL 3068, whereas that seen in ALMA molecular observations extend from $\simeq 1''$ up to $\simeq 10''$ (Kim & Taam 2012; Kim et al. 2017).

The innermost regions of the polar images in Figure 2 of the three PNe are dominated by the emission from their inner rims and nebular envelopes. The ring-like features are clearly detected outside the main nebular shells. These show notable wave-like patterns, which are additionally distorted by collimated protrusions arising from the inner rims and nebular envelopes. These same wave-like patterns are present in the polar image of AFGL 3068, particularly for the outermost regions of the spiral pattern. However, whereas the linear increase of radius with θ prevails here, such trend can only be hardly identified in specific regions of the polar images of the PNe. It can be concluded that the ring-like features of these PNe do not follow the trend to increase their radius with θ as in Archimedean spirals, yet their shapes also depart from that of perfect circles.

Furthermore, the width and spacing of the rings of PNe change with position angle (PA). This is revealed in the enhanced images of NGC 6543, NGC 7009, and NGC 7027 in Figure 1, where the rings towards the West of NGC 6543, North-Northwest of NGC 7009, and East-Northeast of NGC 7027 are sharper than those along the opposite directions, respectively. This is illustrated into further detail for the case of NGC 6543 in Figure 3, which shows surface brightness radial profiles of the region including rings extracted from the *HST* ACS F502N [O III] image along opposite directions of particular interest at PA 70° and 250°. Up to 4 rings can be detected in these spatial profiles (Fig. 3-top), with the Eastern rings at PA 70° being broader than the Western ones at PA 250°, which are brighter and sharper. The basal emission from these surface brightness profile can generally be described by an $r^{-3.6} - r^{-3.4}$ decline, in close agreement with the $r^{-3.3\pm0.1}$ fit found by Balick et al. (2001). After subtracting this basal emission (middle and bottom panels in Fig. 3), the residuals reveal more clearly the rings. The Western rings are indeed sharper and brighter, but these plots also disclose that the radial distances of rings located along opposite directions are not coincident. Measurements of rings distances to the CSPN made on spatial profiles extracted along several directions indicate that the inter-ring spacing of the Western rings is smaller and more coherent, $2\farcs6\pm0\farcs3$, than that of the the Eastern rings, $3\farcs0\pm0\farcs7$. It is pertinent to remark that these asymmetries cannot arise from the interaction with the interstellar medium caused by the proper motion of the CSPN, as these ring-like features are found inside much larger round haloes whose shapes argue against such interactions (Middlemass et al. 1989; Moreno-Corral et al. 1998; Navarro el al. 2003). Interestingly, these asymmetries result naturally in eccentric binary interactions during the AGB (Kim, Liu & Taam 2019).

[1] http://hla.stsci.edu/

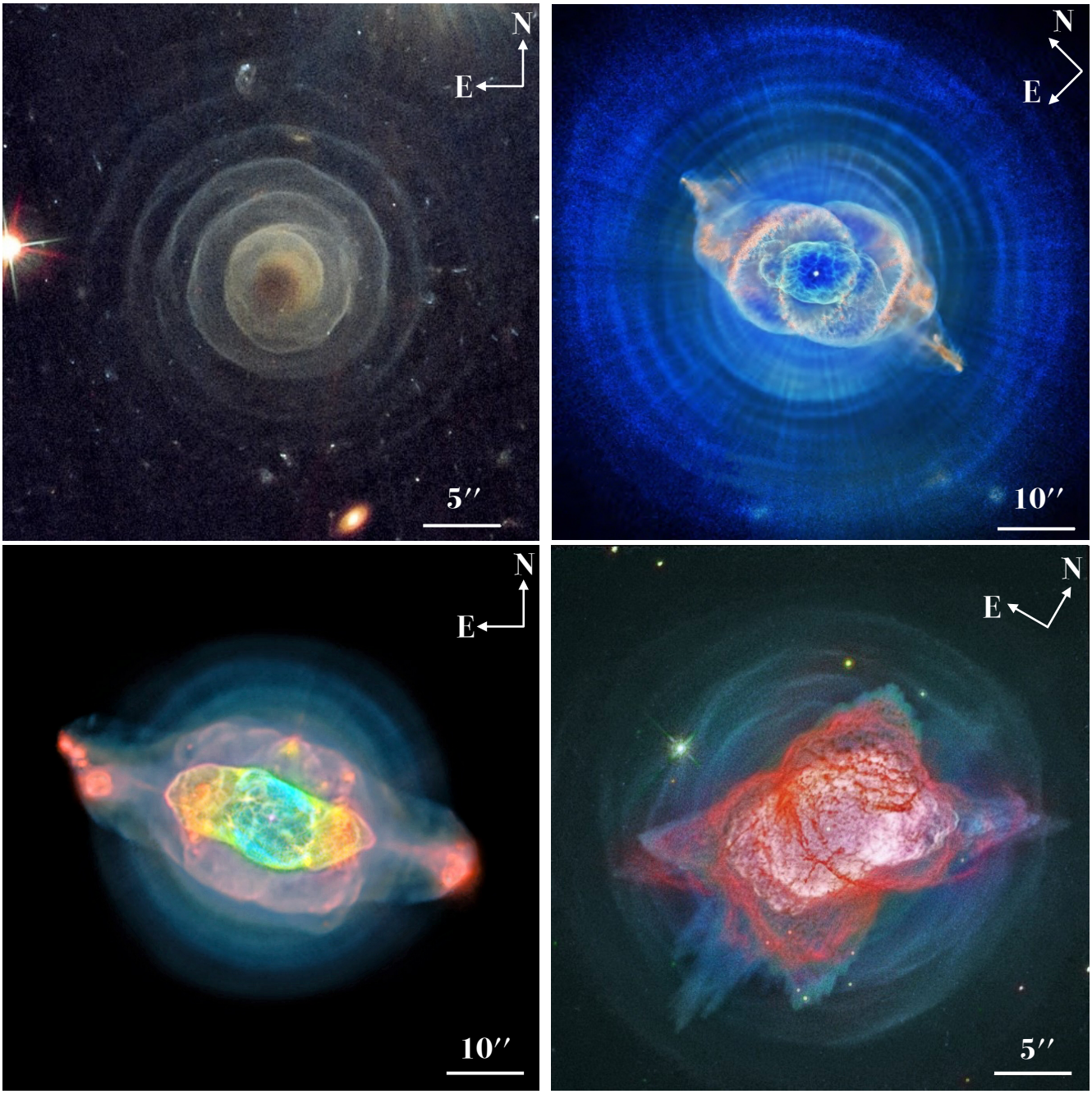

Figure 1. Colour-composite images of AFGL 3068 (top left), NGC 6543 (top right), NGC 7009 (bottom left) and NGC 7027 (bottom right). The original images downloaded from the websites https://www.flickr.com/photos/kevinmgill (AFGL 3068), http://hubblesite.org/image/1578/news_release/2004-27 and https://apod.nasa.gov/apod/ap080322.html (NGC 6543), https://www.eso.org/public/spain/images/eso1731a and https://www.spacetelescope.org/images/opo9738g (NGC 7009), and https://apod.nasa.gov/apod/ap180109.html (NGC 7027) were combined and processed to enhance low surface-brightness features. These low surface-brightness external features are best seen in the broad-band *HST* F606W and F555W filters for AFGL 3068 and NGC 7027, respectively, but in the narrow-band *HST* F502N filter for NGC 6543 and NGC 7009.

The radial profiles of the outer regions of NGC 6543 shown in Figure 3 can also be used to investigate whether these rings broaden with their radial distance from the CSPN. Gaussians fits to these profiles find that their widths consistently increase from the innermost to the outermost ring-like features shown in these profiles by ∼18% in the Western side and by ∼47% in the Eastern side. We note that a small fraction of this broadening may be caused by the average over large spatial regions resulting from the wedge-shaped aperture used to derive these profiles given the low signal-to-noise ratio of the emission from these features. A detailed analysis of the broadening of rings with radial distance in a meaningful sample of

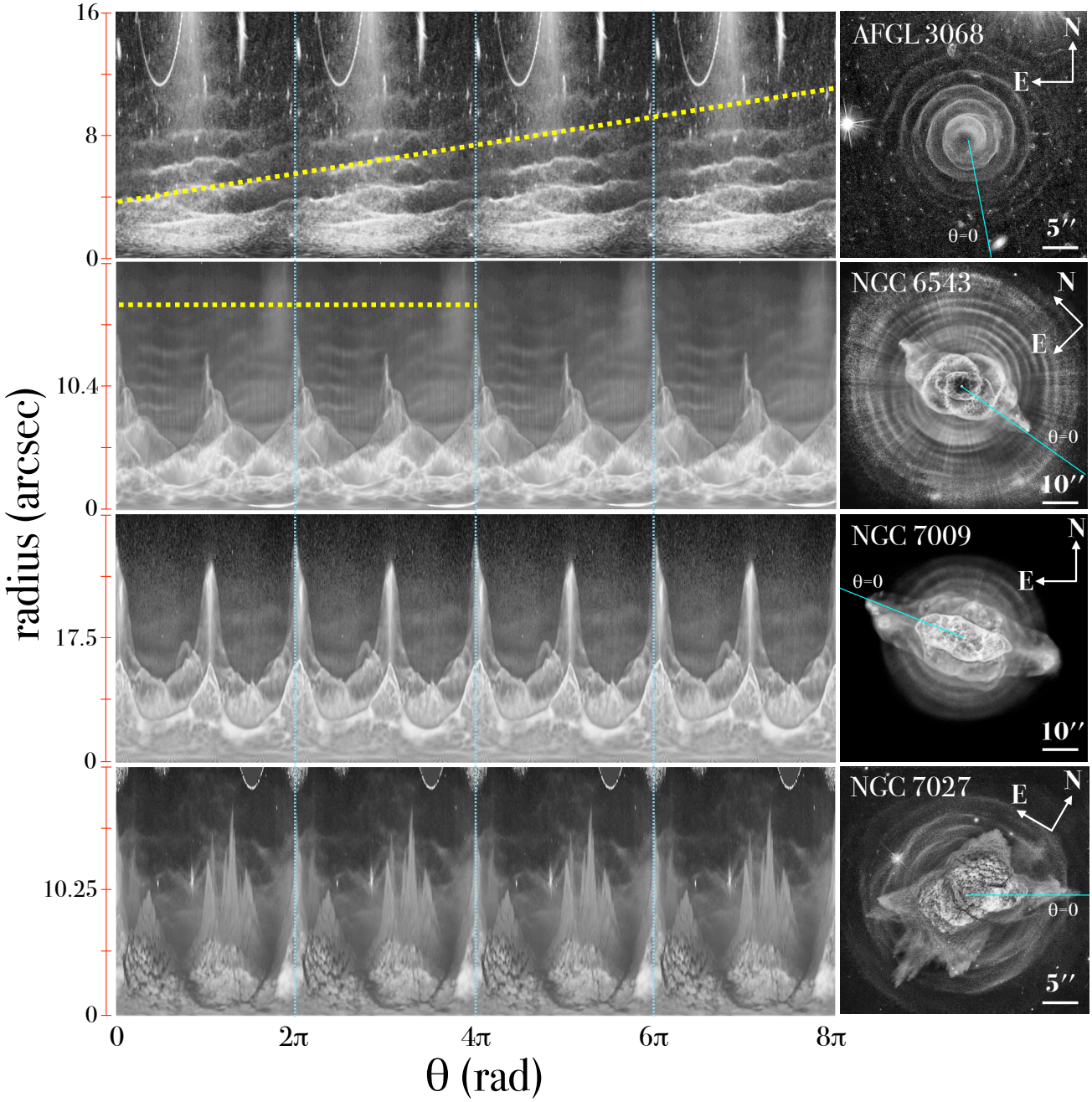

Figure 2. (left) *HST* images of AFGL 3068, NGC 6543, NGC 7009, and NGC 7027 presented in polar $(r - \theta)$ coordinate space, where each column has been computed from a wedge-shaped region with aperture angle of 2° for AFGL 3068 and 1° for the three PNe. The vertical extent of these panels is 16.″0, 20.″8, 35.″0, and 20.″5, respectively. The angular coordinate is replicated 4 times to emphasize the angular trends. The vertical dotted lines mark the 2π, 4π, and 6π lines. The dotted yellow lines overlaid on the polar plots of AFGL 3068 and NGC 6543 show the pattern expected for an Archimedean spiral and a circular shell, respectively. (right) Direct images of each object, which are grayscale representations of the images in Figure 1. The angular coordinate θ increases counter-clockwise and its origin is labeled.

PNe with deep *HST* observations is mandatory to strengthen this tantalizing result.

4 TIME EVOLUTION OF THE RINGS

Multi-epoch *HST* images can be used to assess the surface brightness variations and angular expansion of the ring-like features of the PNe NGC 6543 and NGC 7027 and the spiral pattern around AFGL 3068 for which suitable multi-epoch datasets are available. NGC 7009 is thus excluded from the subsequent analysis in this sec-

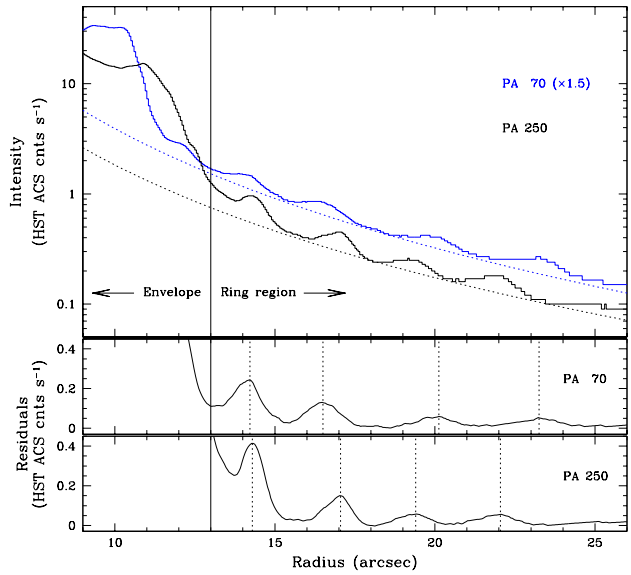

Figure 3. [O III] surface brightness profiles of the Cat's Eye Nebula (NGC 6543) extracted from the *HST* ACS F502N image. The top panel shows the radial surface brightness profiles extracted along PAs 70° (blue histogram) and 250° (black histogram), where the former has been multiplied by 1.5 to make easier the comparison of both profiles. These are obtained using wedge-shaped apertures along these PAs with aperture angle of 10° to improve the signal-to-noise ratio at large radii. The solid vertical line marks the border between the envelope-dominated region of the surface brightness profile and the region where rings are clearly detected. The dashed lines show the $r^{-3.6}$ (blue line) and $r^{-3.4}$ (black line) fits to these surface brightness profiles. The residuals of these fits are shown in the bottom panels for the two PAs. The vertical dashed lines in these panels mark the radial location of each ring.

tion. As noted in §2, only images obtained with the same *HST* camera and filter have been analysed here to avoid instrumental effects. The time-lapse between images is Δt = 6.09 yr for AFGL 3068, 5.99 yr for NGC 6543, and 12.98 yr for NGC 7027. The possible variations in the surface brightness profiles and the general angular expansion caused by the time evolution of the ring-like features of PNe and the spiral pattern around AFGL 3068 are investigated in the next two sections.

4.1 Surface Brightness Variations

To investigate the surface brightness variations of the outermost structures of these sources, we have extracted radial profiles along clean directions from images obtained at two different epochs and compare then in Figure 4. A preliminary inspection does not reveal any obvious difference in the surface brightness radial profiles along these directions. These are examined more carefully at the bottom of each panel of Figure 4, where the surface brightness radial profiles of different epochs have been subtracted. The residuals (shown in red in these figure) are generally flat, indicating that no noticeable changes in the surface brightness radial profiles are detected in timescales of a few years. Significant variations appear in the innermost regions of NGC 6543 and NGC 7027 (not shown in the figure), but these are attributed to the expansion of the inner nebular shell. Otherwise, the small fluctuations seen at the location of some rings are due to their expansion between different epochs. This expansion will be examined into further detail next.

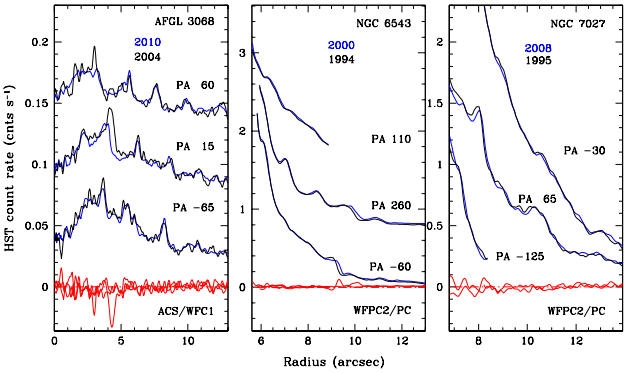

Figure 4. Comparison of multi-epoch surface brightness profiles (blue and black lines) of AFGL 3068, NGC 6543, and NGC 7027 along the different radial directions labeled on each panel obtained using wedge-shaped apertures with aperture angle of 2°. Profiles along different directions have been shifted vertically to improve the readibility of the figure. The difference between each profile is shown by the red lines at the bottom of each panel.

4.2 Angular Expansion

The comparison of different epoch high-quality images with stable point-spread function (PSF) of PNe, as those obtained by *HST*, has been used to confirm and measure the angular expansion rate of their bright rims and nebular envelopes (see Schönberner, Balick & Jacob 2018, and references therein for the most recent use of this method). The direct use of this technique to the arc-like features in the haloes of PNe and spirals around AGB stars is hampered by their extended, diffuse morphology, their weakness, and the steep surface brightness profile of the emission from the PN halo.

To assess the expansion of these features in AFGL 3068, NGC 6543, and NGC 7027 we have adopted the magnification method applied by Schönberner, Balick & Jacob (2018) with the refinement introduced by Santamaría et al. (2019) to measure the expansion of the nova shell IPHASX J210204.7+471015. Basically, the images from different epochs have been aligned using the central stars of NGC 6543 and NGC 7027, and galaxies in the field of view for AFGL 3068, and the older image is then magnified in steps as small as 0.01%, its flux scaled to that of the newest image, and subtracted from the latter. The count number standard deviation of the pixels inside the rectangular apertures shown in the left panels of Figure 5 are then computed. These apertures have typical sizes of 1.″0–1.″5 by 4″–7″ and are oriented along the arc-like features of NGC 6543 and NGC 7027 and the spiral arms of the pattern around AFGL 3068. They trace the sharpest features registered in the images obtained at different epochs, avoiding field stars and hot pixels or any other image blemish. We note that some apparent sharp features are unfortunately affected by image imperfections or have not been registered by the observations obtained at the two different epocs. These have been disregarded from further calculations. The standard deviation of the pixels inside these rectangular apertures, when plotted against the angular offset of the oldest image (i.e., the magnification factor times the radial distance of the rectangular aperture to the CSPN) reveals typical patterns that decrease, reach a minimum value, and then increase (Appendix A). The minimum value of these curves has been used to determine the angular offset that best fit the angular expansion of the feature inside each rectangular aperture.

The angular expansion rate of the ring-like features of NGC 6543 and NGC 7027 and the spiral pattern of AFGL 3068

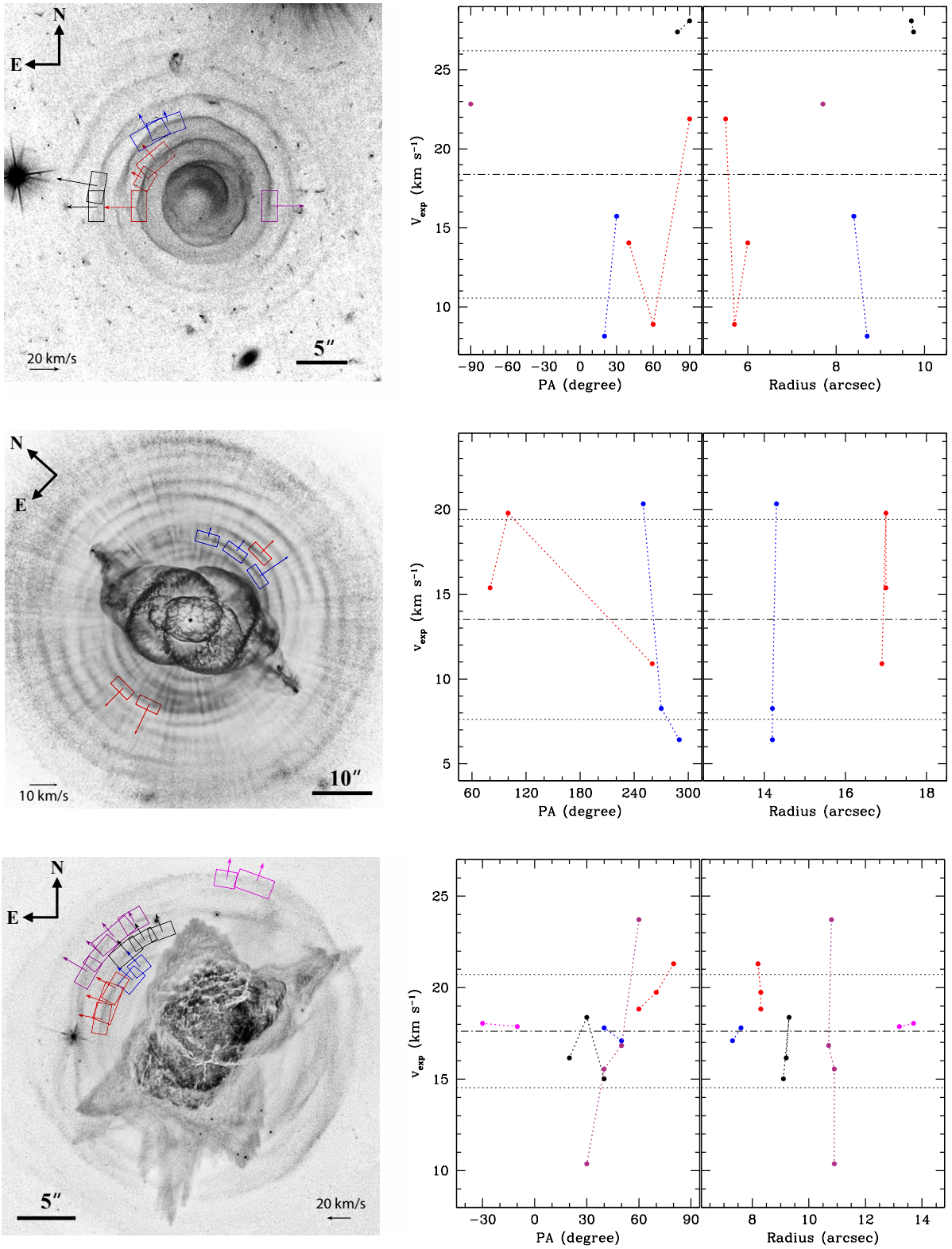

Figure 5. (*left*) Grayscale representations of the images of AFGL 3068 (*top*), NGC 6543 (*middle*), and NGC 7027 (*bottom*) in Figure 1 showing the rectangular apertures used to derive the expansion velocities of ring-like features and arms of spiral patterns. Velocity vectors are represented by arrows with length proportional to the expansion velocity. The color of the rectangular boxes on each image denotes different arc-like features and spiral arms. (*right*) Plots showing the dependence of the expansion velocities of rings and spiral arms of these nebulae with respect to the PA and radial distance to their central stars. The color of each data point matches that of the rectangular boxes enclosing it in the corresponding image in the left panel. Data points associated to a same arc-like feature or spiral arm are connected by dotted lines of the same color.

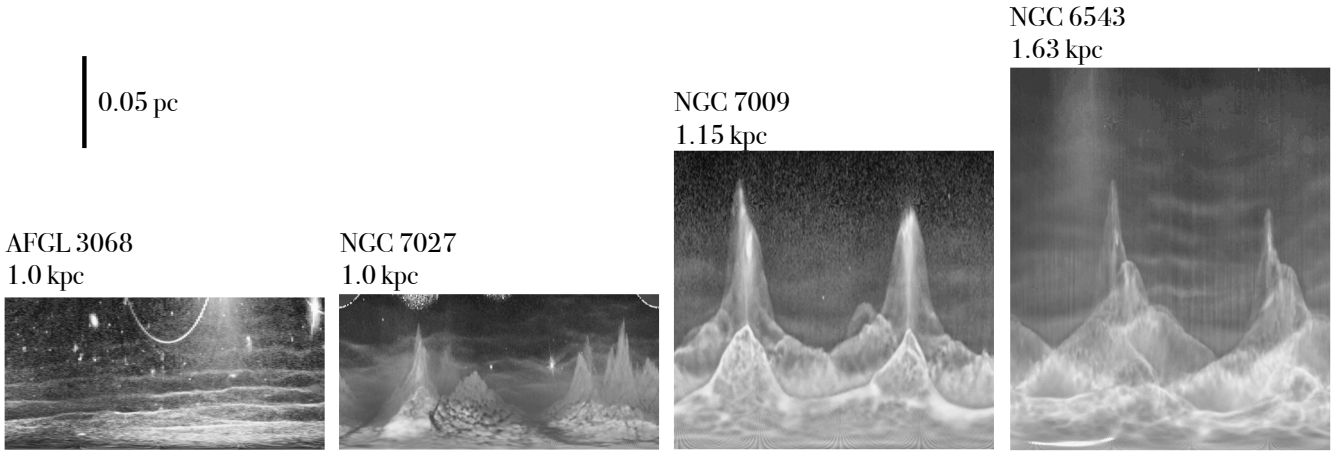

Figure 6. Polar images of AFGL 3068, NGC 7027, NGC 7009, and NGC 6543. This is a revision of Figure 2, where the radial sizes have been transformed to physical scale as indicated by the vertical bar according to the distance to each source.

at the location of these apertures can be computed from this best fit angular offset and the time-lapse between the different epoch images. Adopting the distances to each source listed in Table 1, the expansion velocities at these locations can be derived. These are shown by arrows in the left panels of Figure 5. The possible dependence of the expansion velocity with PA or radial distance is investigated in the right panels of Figure 5, but results are inconclusive: all measurements are within 1-σ deviation (the dotted lines in these plots) of the averaged values of the expansion velocity on the plane of the sky (the dotted-dashed lines). These are 18±8 km s^{-1} for AFGL 3068, 13.5±6 km s^{-1} for NGC 6543, and 17.6±3.1 km s^{-1} for NGC 7027. The expansion velocities derived for these features imply relatively coherent time-lapses between concentric features: 530±150 yr for AFGL 3068, 1900±1100 yr for NGC 6543, and 520±140 yr for NGC 7027. Previous estimates of these for AFGL 3068 and NGC 6543 yield 800 and 1500 yr, respectively (Kim et al. 2017; Balick et al. 2001).

5 FROM REGULAR PATTERNS AROUND AGB STARS TO ARCS AROUND PNE

The prevalence of incomplete rings and arcs outside the nebular core of PNe was evidenced in Paper I. On the contrary, the occurrence of spiral patterns (Kim & Taam 2012; Decin et al. 2015; Kim et al. 2017; Homan et al. 2018) and regular shells (González Delgado et al. 2001; Mauron & Huggins 2006) among AGB stars is quite significant. The analysis of the *HST* images of AFGL 3068, NGC 6543, NGC 7009, and NGC 7027 presented in previous sections provides us with interesting hints to understand the connection and possible evolution between the regular patterns surrounding AGB stars and irregular arcs around PNe.

The expansion velocity on the plane of the sky of the spiral pattern around AFGL 3068 derived from multi-epoch *HST* images of dust-scattered light in the previous section (18±8 km s^{-1}) is consistent with the radial velocity expansion derived from ALMA data of CO molecular emission (14 km s^{-1}; Kim et al. 2017), indicating that the same expansion pattern is detected by these independent methods. This expansion velocity is similar to that measured in the spiral patterns and shells around AGB stars such as EP Aqu (14 km s^{-1}; Homan et al. 2018), IRC+10216 (14.5 km s^{-1}; Cernicharo et al. 2015), RW LMi (16 km s^{-1}; Kim et al. 2015), and R Scu (15 km s^{-1}; Maercker et al. 2012), suggesting that this is a typical expansion velocity for material expelled during this phase of stellar evolution (Ramstedt et al. 2009; Ivezić & Elitzur 2010). The expansion velocities of the arc-like features around NGC 6543 (13.5±6 km s^{-1}) and NGC 7027 (17.6±3.1 km s^{-1}) are within a similar velocity range. Certainly the statistics is very poor, but there is no reason for the time being to reject the hypothesis that the incomplete features seen in the outer shells of PNe result from the evolution of regular patterns around AGB stars.

The similarity between the time-lapse derived for concentric features in NGC 6543 and NGC 7027 and those derived in AGB stars reinforces this hypothesis. The time-lapse between concentric features in NGC 6543 and NGC 7027 are 1400±1100 yr and 520±140 yr, respectively, whereas in AGB stars these are derived to be 530±150 yr (this work) and 800 yr (Kim et al. 2017) in AFGL 3068, 800–1000 yr in IRC+10216 (Cernicharo et al. 2015), and 350 yr in R Scu (Maercker et al. 2012), but notably smaller ≃50 yr in EP Aqu (Homan et al. 2018). This comparison is statitically strenghtened with the large sample of proto-PNe and PNe analyzed in Paper I, that revealed time-lapses for these sources in the range from 90 to 2000 yr.

If the regular patterns present in the stellar wind of AGB stars evolve into the irregular, incomplete concentric patterns detected in PNe, these morphological changes should arise as the result of their expansion and of their interaction with the post-AGB stellar winds and ionization or excitation by the increased UV photon flux from the CSPN. These are investigated in the next sections.

5.1 Size Matters

We present in Figure 6 a comparison of the physical size of AFGL 3068, NGC 6543, NGC 7009, and NGC 7027 using images in polar coordinates. The different panels, corresponding to different sources, reveal that the outermost structures detected in AFGL 3068 have similar physical sizes to the innermost of these structures detected in PNe, whereas the outermost features of the most evolved sources, NGC 6543 and NGC 7009, have sizes about twice larger than those of AFGL 3068.

The farthest regions of the spiral pattern of AFGL 3068 traced by the *HST* image show noticeable kinks with amplitude increas-

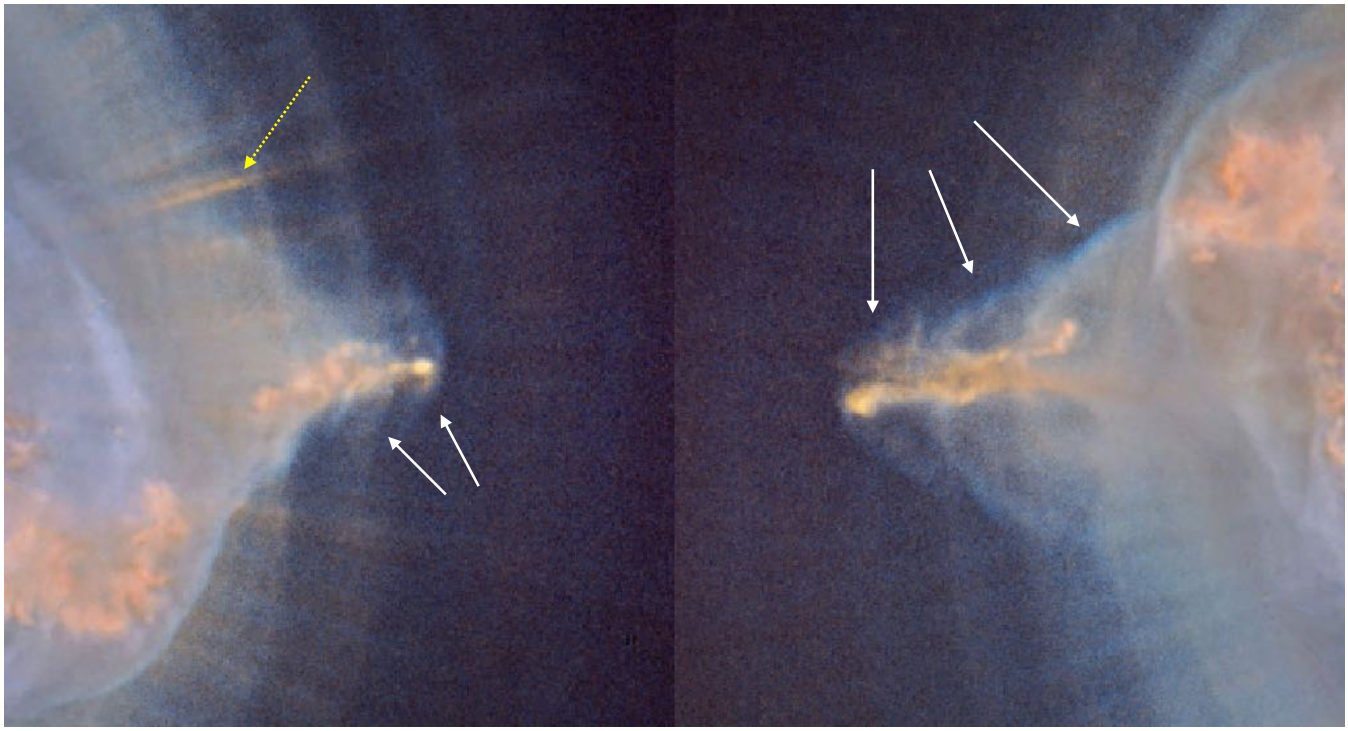

Figure 7. Colour-composite pictures in Hα (green), [O III] (blue) and [N II] (red) of the interaction regions between the bipolar jets of NGC 6543 and the ring-like structures surrounding the nebular shell. White arrows point to bow-shock-like features resulting from the progression of the bipolar jets through the ring-like structures, whereas the yellow arrow marks a radial structure of lower ionization degree across these ring-like features.

ing with radial distance to the central star. Actually, the outermost features of AFGL 3068 look more similar to the arcs and ring-like features of these three PNe than to the almost perfect Archimedean spiral in ALMA observations (Kim et al. 2015) and the innermost regions of the spiral pattern in the *HST* image. At least for AFGL 3068, there is a trend for the regular AGB pattern to get distorted in shape as its distance from the central star (and thus its age) increases. This can be expected as initial velocity fluctuations gets amplified in time with the expansion of the spiral pattern (Kim, Liu & Taam 2019).

Adopting the average expansion velocity derived from their angular expansion in §4.2, the age of the features closest to the central stars is ~700 yr for AFGL 3068, ~6,000 yr for NGC 6543, and ~2,000 yr for NGC 7027. If these features expanded thermally, they should thicken as they age, thus these relatively large ages, particularly for NGC 6543 (but also for other sources in Paper I, with ages up to 4500 yr), would imply a noticeable broadening of the rings. Indeed, the width of the "younger" features around AFGL 3068 are sharper than the "older" features around NGC 6543 in Figure 6. Considering the distance to both sources, the spiral arms around AFGL 3068 have a width (σ) of $(3.6\pm1.1)\times10^{15}$ cm, whereas the Western arc-like features around NGC 6543 have a width of 1.5×10^{16} cm and the Eastern ones have a width of 1.8×10^{16}, i.e., 4–5 times broader than those of AFGL 3068. There is no clear variation of the width of the spiral arms around AFGL 3068 with their radial distance to the CSPN, but there is a tantalizing indication that the ring-like features around NGC 6543 thicken as they propagate outwards.

5.2 Breaking Bad

The inner regions of the polar images of NGC 6543, NGC 7009, and NGC 7027 presented in Figures 2 and 6 also reveal the progression of the inner rims, nebular envelopes and collimated outflows throughout the outer ring-like features. The outer edge of the nebular envelope drives a shock into the AGB wind, which is detected through its enhanced [O III] to Hα ratio (Guerrero et al. 2013). Any feature in the AGB wind is swept up and destroyed wherever the nebular envelope reaches them.

Similarly, the expansion of collimated outflows has deep dynamical and morphological effects on the ring-like features as shown in Figure 7 for the case of NGC 6543. The bipolar jets progress through the ring-like structures surrounding the nebular shell and produce a series of bow-shock-like features (the most noticeable ones are marked with white arrows in Fig. 7), which can be associated with each of these ring-like structures. Similar features are detected in the image of NGC 7009. Apparently, the bipolar jets break through a region of enhanced density every time they cross the boundary of a ring-like features. As the ambient gas is deflected from the collimated outflow tips, it becomes hot and its increased thermal pressure produces a bow-shock-like feature at the leading tip, while the gas left in the wake cools adiabatically as it slows down (Balick el al. 2013). Since the bipolar jets in NGC 6543 are not contained on the plane of the sky (Miranda & Solf 1992), this confirms that the arcs and incomplete rings around NGC 6543 are the projection of 3D structures. Even if these are 3D structures and this interaction takes place only at a given inclination angle, their effects in the morphology are quite noticeable.

5.3 Testing the Survival of Regular AGB Patterns

There is a large number of high-quality 3D numerical works addressing the formation and evolution of regular structures and very specifically spiral patterns by common envelope binary interactions or eccentric binary interactions during the AGB phase (see Chamandy et al. 2018; Iaconi et al. 2018; Kim, Liu & Taam 2019, and references therein). However, none of these simulations explore the effects on these structures caused by the increase of the UV flux from the central star and the mechanical luminosity and linear momentum of its stellar wind during the post-AGB phase. These effects were explored using 1D simulations by Meijerink et al. (2003), who found that the ionizing photon flux from the CSPN is capable to erase the signature of regular structures within a few thousand years.

The alternating rays of ionized material intersecting the ring-like features and arcs of NGC 6543 and NGC 7009 (Fig. 1 and yellow arrow in Fig. 7) reveal that the effects of ionizing photon flux from the CSPN are far from isotropic. These rays of ionization arise from shadow effects (see Arthur & Hoare 2006; Williams 1999) caused by clumps and filaments produced as the result of Rayleigh-Taylor and thin-shell instabilities in the wind-wind interaction region (e.g., Stute & Sahai 2006; Toalá & Arthur 2016) as these clumps trap the ionizing UV flux from the CSPN preventing the ionization to be uniform. These are effects that can be noticeable even before the onset of ionization, as illustrated by the fragmented arc segments in the proto-PN CRL 2688 (Balick et al. 2012).

These are effects that cannot be modeled using 1D simulations (as those presented by Meijerink et al. 2003) and are specifically investigated here via radiation-hydrodynamic simulations using the code described in Toalá & Arthur (2011) and Arthur (2012). Here we will adopt a simplified mass-loss rate history for the last 10^5 yr in the AGB phase with a basal mass-loss rate of $\dot{M}$=10^{-5} M$_\odot$ yr^{-1} and a constant wind velocity of $v_{\rm AGB}$=15 km s^{-1} suitable for a 1.5 M$_\odot$ progenitor (Vassiliadis & Wood 1993, 1994; Blöcker 1995). In the last 20,000 yr of evolution, the mass-loss rate is artificially enhanced by an order of magnitude during 200 yr every 1500 yr to create density enhancements between the rings and inter-ring regions. The duration and period have been adopted to fit the surface brightness variations observed in the ring-like features around NGC 6543 (Fig. 3). The density enhancement of an order of magnitude has been adopted to match the apparent "mass-loss fluctuations" from a few up to several hundreds, with time-lapses of a few hundred years due to quasi-periodic mass loss caused by dust drift on the otherwise constant AGB mass-loss (Simis et al. 2001). Density enhancement from a few up to one hundred in exceptional cases are also found by Kim, Liu & Taam (2019) for the spiral and inter-spiral regions in their simulations caused by the eccentric-binary interactions during the AGB. Observational determinations of the density contrasts are also in the range 3–10, as reported for the regular structures surrounding the AGB stars CW Leo and IRC +10 218 (Decin et al. 2015; Guélin et al. 2018).

The mass-loss rate history and the evolution of the stellar wind velocity with time used in our simulation are shown in Figure 8. These are used to produce 1D calculations with 2000 uniformly spaced radial cells that correspond to 0.5 pc in spatial size, i.e., 2.5×10^{-4} pc per cell, where the wind injection zone comprises the innermost 10 cells. No photoionization is considered during this phase. The final density profile at the end of the AGB phase exhibits the typical $\rho \propto r^{-2}$ distribution (see, e.g., Villaver et al. 2002; Perinotto et al. 2004; Toalá & Arthur 2014, and references therein) with density enhancements overimposed. Although mass loss pulses are assumed to be periodic, the separation between the density enhancements in our simulations is rather quasi-periodic. This occurs because the material ejected during the late AGB phase, and particularly that corresponding to each pulse of enhanced mass loss, interacts hydrodynamically with the material previously ejected. As a result, the distance between each pulse of enhanced mass loss is reduced and their separation is not strictly regular.

To study the hydrodynamical effects at the wind-wind interaction zone and ionizing flux in the post-AGB phase, we remapped the 1D distributions of density, momentum and total energy at the end of the AGB phase into 2D cylindrically symmetric grids. Using these as initial conditions, we obtained 2D simulations injecting an evolving post-AGB wind and ionizing photon flux from an 1.5 M$_\odot$ progenitor star model (Toalá & Arthur 2014). The 2D axisymmetric numerical simulations are performed on a fixed grid of 1200 radial by 2400 z-direction cells of uniform cell size and total grid spatial size of 0.3×0.6 pc^2, i.e., the 1D and 2D simulations have the same radial resolution. The free-wind injection zone has a radius of 40 cells, which corresponds to the innermost 0.01 pc. The 2D simulations start at t = 0 with the injection of the post-AGB (fast) wind (Figure 8). Our numerical results will focus on the innermost 0.3 pc of the PN where the rings are distributed (Fig. 6). This means that we do not follow the evolution of the ionized nebular shell as it leaves the computational domain. Note also that, even though the calculations are performed in a full $r-z$ plane, we only show half of the computational domain.

In the simulations, the fast wind from the post-AGB phase expands into the slow previously ejected AGB material, leading to the creation of a two-shock pattern: the outer shocks sweeps and compresses the AGB material, while the inner shocks thermalises the fast wind creating a diffuse and hot inner bubble (Dyson & Williams 1997). Since the density is higher close to the star, the opacity is also higher and the ionization front is initially trapped close to the inner rim. As the inner rim expands, the opacity drops, allowing the photon flux to move outwards, but clumps formed at early times at the wind-wind interaction layer due thin shell instabilities corrugate the inner rim, producing variations in the opacity and shadowing instabilities (Williams 1999; Arthur & Hoare 2006).

Figures 9 shows three snapshots of the total number density n, gas velocity v, and normalised Hα volume emissivity $j_{\rm H\alpha}$ derived from the 2D numerical simulations at times 2000, 4000, and 6000 yr to illustrate the effects that the variations in opacity produce in the early, mid-age and late evolution of external thin shells of enhanced density. We note that the formation of clumps in the wind-wind interaction at certain angles is actually induced by numerical artifacts of the Cartesian grid used in axisymmetric codes, as the spherically symmetric wind gas flows across square cell boundaries. Whereas the spatial distribution of these clumps should be considered non-relevant, their varying opacities and the effects of the shadowing instabilities that they cause on the interaction of the ionizing flux with the external rings are robust results of these simulations. In early evolutionary phases (t = 2000 yr), when the inner shell opacity is still high, the outer rings keep their initial structure. Later on, when clumps form and the ionization is not isotropic any longer (= 4000 yr), streaks of ionized material and shadowing cones start modifying the inner rim and the AGB material (see García-Segura et al. 1999), in particular the rings. Whilst the precise angular distribution of ionizing streaks and shadowing cones is not indicative of their true spatial locations, their varying intensities allow us to probe different degree of clumpiness in the wind-wind interaction layer. In late phases, when the inner rim becomes more unstable

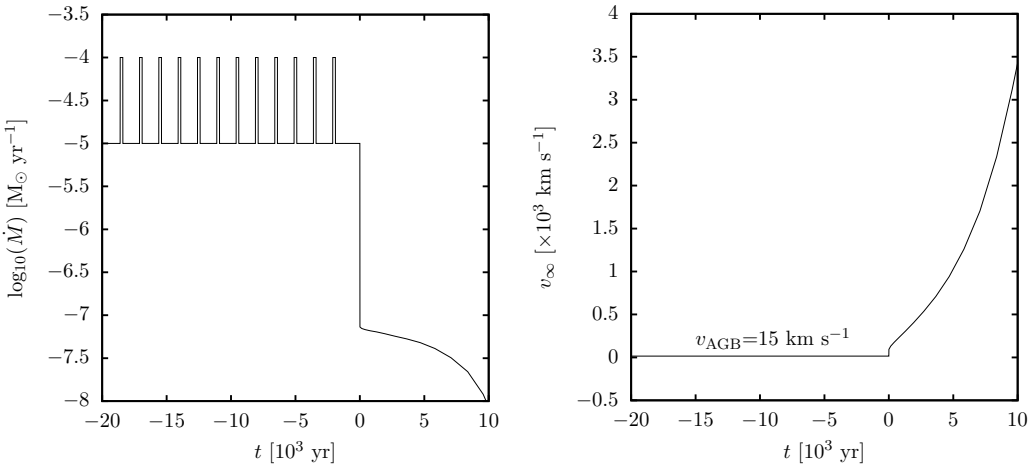

Figure 8. Mass-loss rate $\dot{M}$ (left) and stellar wind velocity v_∞ (right) as a function of time from the onset of the post-AGB wind.

and Rayleigh-Taylor instabilities start to dominate (t = 6000 yr), resulting in dense, finger-like structures pointing inwards, initial rings are broken into independent arcs. The dynamical effects induced by these processes also produce spatial variations in the velocity field (middle panel of Figure 9), with independent arcs resulting from the break-up of the rings by the ionization streaks expanding with different velocities.

The simulations presented above show that the effects of clumps formed at the wind-wind interaction zone trapping the ionizing flux during the post-AGB phase can indeed distort coherent structures formed at the end of the AGB, effectively splitting them apart into independent arcs rather than completely erasing them as predicted in 1D simulations (e.g., Meijerink et al. 2003). Preliminary models for different initial masses of the progenitor and properties of the mass-loss gasps during the AGB (mass loss rate, duration, and period) are suggestive of a wealth of outcomes and timescales. A comprehensive investigation of different initial conditions will be subject of a subsequent study (Toalá et al., in preparation, Paper III). The effects of anisotropic illumination and ionization patterns resulting from shadowing instabilities are expected to dilute in 3D regular patterns, but projection effects will be important. Furthermore, these disruptive processes will add to the noticeable spatial and kinematic asymmetries of the 3D spiral structures proposed to arise in the interaction of a binary system. Modelling the evolution of 3D spiral patterns since their formation in the late AGB to the post-AGB phase, accounting for non-isotropic ionizing flux at that time, will be the topic of future investigations.

6 CONCLUDING REMARKS

We have investigated the detailed morphology and expansion velocity of the spiral pattern around the AGB carbon-rich star AFGL 3068 and the ring-like features around the PNe NGC 6543, NGC 7009 and NGC 7027 using high-quality multi-epoch *HST* images to shed light onto the possible evolutionary connection between these features. AFGL 3068, as some other AGB stars, shows a complete, regular spiral structure around it, whereas the PNe here considered, as all other proto-PNe and PNe, present incomplete ring-like features and arcs. However, the spiral pattern around AFGL 3068 and the arcs around these three PNe have similar expansion velocities, linear sizes, and inter-lapse times. This agreement is supported by detailed studies of a number of AGB stars and a statistical investigation of a large sample of proto-PNe and PNe with similar features (Paper I), suggesting that the ring-like features in PNe may evolve from the regular patterns of AGB stars. A statistical investigation of the kinematics of these features is certainly needed to strenghten this idea.

Interestingly, the spiral pattern around AFGL 3068 gets distorted as material gets older and expands further out from the central star as shown in recent hydrodynamical simulations (Kim, Liu & Taam 2019). These effects are to be added to those resulting from the onset of the post-AGB phase, including the expansion of the PN within the AGB wind and the injection into it of an anisotropic ionizing flux. We witness the interaction of the ring-like features around these PNe with the nebular shells and collimated outflows, as they expand and drive shocks that sweep up the material ejected during the AGB phase. We demonstrate using radiative-hydrodynamic simulations of PN formation that instabilities in the wind-wind interaction region produce anisotropies in the ionizing pattern of the material ejected during the AGB phase. This has important dynamical effects in the evolution of regular patterns imprinted in the AGB material, which get distorted and finally erased during the post-AGB phase.

If this were the case for the ring-like features around NGC 6543, NGC 7009, and NGC 7027, it would not be possible to unambiguosuly attribute them to previous spiral patterns. Interestingly, the inter-ring spacing at one side of each of these PNe is smaller and more coherent than at the other side, and the rings are sharper. This asymmetry cannot be attributed to the compression of regular imprints in the AGB wind as the PN moves through a dense interstellar medium, since these three PNe are surrounded by much larger round haloes that do not reveal such interactions (Middlemass et al. 1989; Moreno-Corral et al. 1998; Navarro el al. 2003). On the contrary, this asymmetry is naturally explained in the framework of a binary interaction producing spiral patterns with this imprint (Kim, Liu & Taam 2019). On the assumption that the ring-like features around PNe were once spiral patterns, then the time-lapse between these ring-like features is related to the orbital period of binary systems at their hearts.

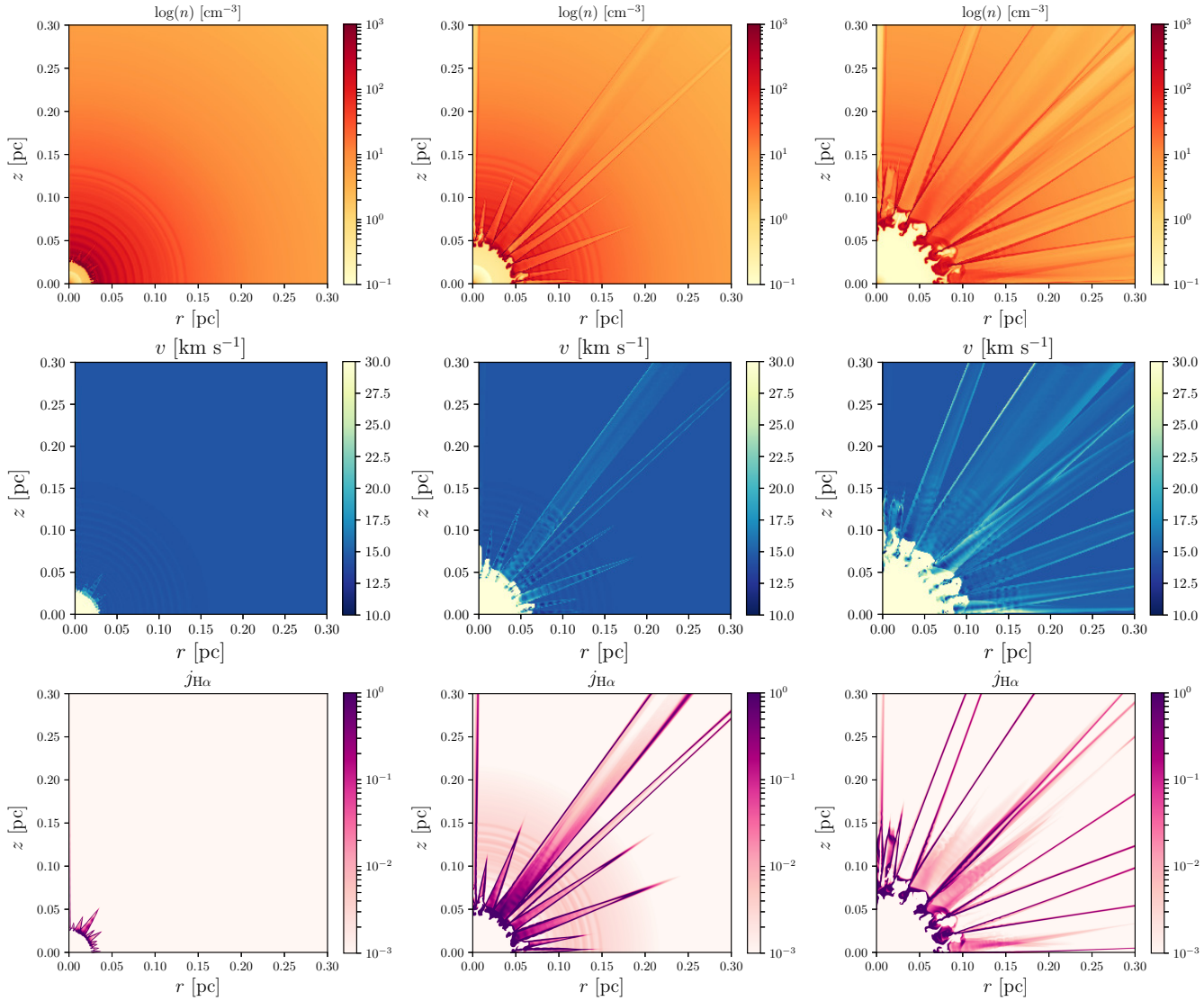

Figure 9. Evolution with time of the total number density n (top panels), gas velocity v (middle panels), and normalised Hα volume emissivity (bottom panels). Left, center, and middle columns correspond to 2000, 4000, and 6000 yr of post-AGB evolution.

ACKNOWLEDGEMENTS

The authors acknowledge support from grants AYA 2014-57280-P and PGC2018-102184-B-I00, co-funded with FEDER funds. JAT and MAG are funded by UNAM DGAPA PAPIIT project IA100318, and LS by UNAM DGAPA PAPIIT project IN101819. GRL acknowledges support from Fundación Marcos Moshinsky, CONACyT and PRODEP (Mexico). BB acknowledges support from program AR-14563 that was provided by NASA through a grant from the Space Telescope Science Institute, which is operated by the Association of Universities for Research in Astronomy, Inc., under NASA contract NAS 5-26555.

This paper is based on observations made with the NASA/ESA *Hubble Space Telescope*, and obtained from the Hubble Legacy Archive, which is a collaboration between the Space Telescope Science Institute (STScI/NASA), the Space Telescope European Coordinating Facility (ST-ECF/ESA) and the Canadian Astronomy Data Centre (CADC/NRC/CSA). The large scale image of NGC 7009 is based on observations collected at the European Southern Observatory by the MUSE science verification team. This work has made extensive use of the NASA's Astrophysics Data System.

REFERENCES

Arthur, S. J. 2012, MNRAS, 421, 1283
Arthur, S. J., & Hoare, M. G. 2006, ApJS, 165, 283
Balick, B. 1987, AJ, 94, 671
Balick, B., Gomez, T., Vinković, D., et al. 2012, ApJ, 745, 188
Balick B., Gonzalez G., Frank A., Jacoby G., 1992, ApJ, 392, 582
Balick B., Huarte-Espinosa M., Frank A., Gomez T., Alcolea J., Corradi R. L. M., Vinković D., 2013, ApJ, 772, 20
Balick, B., Wilson, J., & Hajian, A. R. 2001, AJ, 121, 354
Blöcker, T. 1995, A&A, 297, 727
Cernicharo, J., Marcelino, N., Agúndez, M., & Guélin, M. 2015, A&A, 575, A91
Chamandy, L., Frank, A., Blackman, E. G., et al. 2018, MNRAS, 480, 1898

Corradi, R. L. M., Sánchez-Blázquez, P., Mellema, G., Giammanco, C., & Schwarz, H. E. 2004, A&A, 417, 637
Cox, N. L. J., Kerschbaum, F., van Marle, A.-J., et al. 2012, A&A, 537, A35
Chu, Y.-H., Guerrero, M. A., Gruendl, R. A., Williams, R. M., & Kaler, J. B. 2001, ApJ, 553, L69
Chu Y.-H., Jacoby G. H., Arendt R., 1987, ApJS, 64, 529
Decin L., Richards A. M. S., Neufeld D., Steffen W., Melnick G., Lombaert R., 2015, A&A, 574, A5
Dinh-V. -Trung, Lim J., 2009, ApJ, 701, 292
Dyson, J. E., & Williams, D. A. 1997, The physics of the interstellar medium. Edition: 2nd ed. Publisher: Bristol: Institute of Physics Publishing, 1997. Edited by J. E. Dyson and D. A. Williams. Series: The graduate series in astronomy. ISBN: 0750303069
Frank A., Balick B., Riley J., 1990, AJ, 100, 1903
García-Segura, G., Langer, N., Różyczka, M., & Franco, J. 1999, ApJ, 517, 767
García-Segura, G., López, J. A., & Franco, J. 2001, ApJ, 560, 928
Gómez-Muñoz, M. A., Blanco Cárdenas, M. W., Vázquez, R., et al. 2015, MNRAS, 453, 4175
González Delgado D., Olofsson H., Schwarz H. E., Eriksson K., Gustafsson B., 2001, A&A, 372, 885
Guélin, M., Patel, N. A., Bremer, M., et al. 2018, A&A, 610, A4
Guerrero, M. A., Gruendl, R. A., & Chu, Y.-H. 2002, A&A, 387, L1
Guerrero M. A., Manchado A., 1999, ApJ, 522, 378
Guerrero M. A., Toalá J. A., Medina J. J., Luridiana V., Miranda L. F., Riera A., Velázquez P. F., 2013, A&A, 557, A121
Harpaz, A., Rappaport, S., & Soker, N. 1997, ApJ, 487, 809
Homan W., Richards A., Decin L., de Koter A., Kervella P., 2018, A&A, 616, A34
Iaconi, R., De Marco, O., Passy, J.-C., et al. 2018, MNRAS, 477, 2349
Ivezić Ž., Elitzur M., 2010, MNRAS, 404, 1415
Kastner, J. H., Vrtilek, S. D., & Soker, N. 2001, ApJ, 550, L189
Kim H., Liu S.-Y., Taam R. E., 2019, arXiv e-prints, arXiv:1906.06333
Kim, H., Trejo, A., Liu, S.-Y., et al. 2017, Nature Astronomy, 1, 0060
Kim, H., Liu, S.-Y., Hirano, N., et al. 2015, ApJ, 814, 61
Kim, H., & Taam, R. E. 2012, ApJ, 759, L22
Kwok, S., Su, K. Y. L., & Hrivnak, B. J. 1998, ApJ, 501, L117
Maercker, M., Mohamed, S., Vlemmings, W. H. T., et al. 2012, Nature, 490, 232
Mastrodemos, N., & Morris, M. 1999, ApJ, 523, 357
Mauron, N., & Huggins, P. J. 2006, A&A, 452, 257
Mauron, N., Huggins, P. J., & Cheung, C.-L. 2013, A&A, 551, A110
Mayer A., et al., 2013, A&A, 549, A69
Meijerink, R., Mellema, G., & Simis, Y. 2003, A&A, 405, 1075
Middlemass D., Clegg R. E. S., Walsh J. R., 1989, MNRAS, 239, 1
Miranda, L. F., & Solf, J. 1992, A&A, 260, 397
Moreno-Corral M., de La Fuente E., Gutiérrez F., 1998, RMxAA, 34, 117
Navarro S. G., Corradi R. L. M., Mampaso A., 2003, RMxAC, 75, RMxAC..18
Olofsson H., Bergman P., Eriksson K., Gustafsson B., 1996, A&A, 311, 587
Olofsson H., Bergman P., Lucas R., Eriksson K., Gustafsson B., Bieging J. H., 1998, A&A, 330, L1
Perinotto, M., Schönberner, D., Steffen, M., & Calonaci, C. 2004, A&A, 414, 993
Ramos-Larios, G., Santamaría, E., Guerrero, M.A., Marquez-Lugo, R.A., Sabin, L., & Toalá, J.A. 2016, MNRAS, 462, 610 (Paper I)
Ramos-Larios, G., Phillips, J. P., & Cuesta, L. C. 2011, MNRAS, 411, 1245
Ramos-Larios, G., Vázquez, R., Guerrero, M. A., et al. 2012, MNRAS, 423, 3753
Ramstedt S., Schöier F. L., Olofsson H., 2009, A&A, 499, 515
Sahai, R., Morris, M. R., & Villar, G. G. 2011, AJ, 141, 134
Sahai, R., Trauger, J. T., Watson, A. M., et al. 1998, ApJ, 493, 301
Santamaría E., Guerrero M. A., Ramos-Larios G., Sabin L., Vázquez R., Gómez-Muñoz M. A., Toalá J. A., 2019, MNRAS, 483, 3773
Schönberner D., Balick B., Jacob R., 2018, A&A, 609, A126
Simis, Y. J. W., Icke, V., & Dominik, C. 2001, A&A, 371, 205
Stanghellini L., Pasquali A., 1995, ApJ, 452, 286
Stute, M., & Sahai, R. 2006, ApJ, 651, 882
Su, K. Y. L., Volk, K., Kwok, S., et al. 1998, ApJ, 508, 744
Terzian, Y., & Hajian, A. R. 2000, Asymmetrical Planetary Nebulae II: From Origins to Microstructures, 199, 33
Toalá, J. A., & Arthur, S. J. 2011, ApJ, 737, 100
Toalá, J. A., & Arthur, S. J. 2014, MNRAS, 443, 3486
Toalá, J. A., & Arthur, S. J. 2016, MNRAS, 463, 4438
Vassiliadis, E., & Wood, P. R. 1993, ApJ, 413, 641
Vassiliadis, E., & Wood, P. R. 1994, ApJS, 92, 125
Villaver, E., García-Segura, G., & Manchado, A. 2002, ApJ, 571, 880
Williams, R. J. R. 1999, MNRAS, 310, 789
Zijlstra, A. A. 2015, Rev. Mex. Astron. Astrofis., 51, 221
Zijlstra, A. A., Bedding, T. R., & Mattei, J. A. 2002, MNRAS, 334, 498